

INTERNATIONAL JOURNAL OF
**Lightweight Materials
and Manufacture**

Volume 6, Issue 3 • September 2023

International Journal of Lightweight Materials and Manufacture

EDITORIAL BOARD MEMBERS

EDITORS-IN-CHIEF

Zhiqiang Li

AVIC Manufacturing Technology Institute, China

Jianguo Lin

Imperial College London, UK

ASSOCIATE EDITORS

John Dear

Imperial College London, UK

Paulo Martins

Instituto Superior Técnico, Portugal

Yi Qin

University of Strathclyde, UK

ASSISTANT EDITORS

Haibao Liu

Cranfield University, UK

Kwek-Tze Tan

The University of Akron, U.S.

EDITORIAL BOARD

Bamber Blackman

Imperial College London, UK

Daolun Chen

Ryerson University, Canada

Bhattacharjee Debashish

Tata Steel, India

Livan Fratini

University of Palermo, Italy

Mingwang Fu

The Hong Kong Polytechnical University, Hong Kong, China

Meysam Haghshenas

The University of Toledo, U.S.

Christoph Hartl

Technische Hochschule Köln, Germany

Ghulam Hussain

GIK Institute of Engineering Sciences & Technology, Pakistan

Yun-Jae Kim

Korea University, Korea

Dae-Cheol Ko

Pusan National University, Korea

Zoltan Kolozsvary

S.C. Plasmaterm S.A., Romania

Zbigniew Kowalewski

Polish Academy of Sciences, Poland

Jan Kusiak

AGH University of Science and Technology, Poland

Toshihiko Kuwabara

Tokyo University of Agriculture and Technology, Japan

Zhongqin Lin

Shanghai Jiao Tong University, China

Jian Lu

City University of Hong Kong, Hong Kong, China

Krzysztof Muszka

AGH University of Science and Technology, Poland

Thomas Niendorf

Universität Kassel, Germany

Duc Pham

University of Birmingham, UK

Jean-Philippe Ponthot

Université de Liège, Belgium

Miklós Tisza

University of Miskolc, Hungary

Pan Wang

Singapore Institute of Manufacturing Technology, Singapore

Jer-Ren Yang

Taiwan University, Taiwan, China

Rui Yang

Institute of Metal Research, Chinese Academy of Science, China

Shijian Yuan

Harbin Institute of Technology, China

Lihua Zhan

Central South University, China

Di Zhu

Nanjing University of Aeronautics and Astronautics, China



Original Article

The effects of I-Beam thickness to microstructure and compression load of thin wall ductile iron connecting rod



Rianti Dewi Sulamet-Ariobimo^{a,*}, Muhammad Fadhlan^a, Yoska Oktaviano^a,
Tono Sukarnoto^a, Yusep Mujalis^a, Amal Witonohadi^{b,**}

^a Mechanical Engineering Department, Faculty of Industrial Technology, Universitas Trisakti, Jakarta, 11440, Indonesia

^b Industrial Engineering Department, Faculty of Industrial Technology, Universitas Trisakti, Jakarta, 11440, Indonesia

ARTICLE INFO

Article history:

Received 27 August 2022

Received in revised form

7 December 2022

Accepted 2 January 2023

Available online 18 January 2023

Keywords:

Thin wall ductile iron (TWDI)

Connecting rod

Thickness

Compression load

ABSTRACT

Lighter automotive components are needed to reduce energy consumption. The manufacturing processes of the components should also consume less energy and be environmentally friendly. Aluminum is a lightweight material, but the manufacturing processes consume a lot of energy. Ductile iron has outstanding design flexibility and applying a thin wall casting technique to the ductile iron components will reduce the weight and make it possible for ductile iron to compete with lightweight materials. The achievement of making a 3 mm I-beam thickness connecting rod which fulfills the design requirement in previous research has encouraged a further reduction in the I-beam thickness. This action is taken to enhance the weight reduction gained from the connecting rod. The aims of this work are to ensure the repeatability resulting from the design of 3 mm I-beam thickness and the ability of the casting design to produce the 2 mm I-beam thickness. Solidification rates in thin wall casting are critical due to the differences in thicknesses in the product. It is also to analyze the effect of I-beam thickness on the compression load. Two types of I-beams, which differ in their thickness, 3 mm and 2 mm, were produced in the foundry scale. All the I-beams were characterized by their microstructure and compression load. The compression load was measured using the tensile method. The results of microstructure observations revealed that the microstructure in I-beam is different from the one in the end rod except for one casting position, while the result of compression load shows a similar value for average compression load between the 3 mm and 2 mm which fulfill the compression load requirement of connecting rod. The casting designs built in this research can produce thin wall ductile iron (TWDI) connecting rods that could stand similar load with the original one.

© 2023 The Authors. Publishing services by Elsevier B.V. on behalf of KeAi Communications Co. Ltd. This is an open access article under the CC BY license (<http://creativecommons.org/licenses/by/4.0/>).

1. Introduction

Nowadays, lighter automotive components are produced to reduce energy consumption during their usage. The lighter components should possess the capabilities of the original components in fulfilling the requirement of the design. While it also should be low in production energy, customer, and environmentally friendly

[1]. When it comes to weight reduction, people tend to choose aluminum as the substitute material. Unfortunately, aluminum cannot meet the aspects of low production energy and environmentally friendly. Allwood and Cullen [2] mentioned the number of 170 GJ/tonne as the energy intensity during the production of primary aluminum is GJ/tonne with the emission based on carbon intensity is 10 (tco₂/t). When compared to primary iron/steel, the energy intensity of primary iron/steel making is about 35 GJ/tonne with a 1 (tco₂/t) emission rate. The energy needed for the primary aluminum process is around three times that of primary iron which also produces higher carbon dioxide. Jolly et al. [3] studied the further impact of weight reduction using material replacement in the engine block. They assessed the energy intensity and emission for both aluminum and cast-iron engine block. They found that the decisions about lightweight and fuel saving cannot adequately assess through tail-pipe emissions. Then, when turning to

* Corresponding author.

** Corresponding author.

E-mail addresses: riantiarobimo@trisakti.ac.id (R.D. Sulamet-Ariobimo), m.fadhlan@trisakti.ac.id (M. Fadhlan), yoska@trisakti.ac.id (Y. Oktaviano), tsukarnoto@trisakti.ac.id (T. Sukarnoto), yusep@trisakti.ac.id (Y. Mujalis), amal@trisakti.ac.id (A. Witonohadi).

Peer review under responsibility of Editorial Board of International Journal of Lightweight Materials and Manufacture.

composite, Czerwinsky [4] found that the application of composite structure is generally driven by the trade-off between its light-weight performance with production cost.

Thin wall casting technology has been able to reduce the weight of ductile iron [5] and fulfill the requirement of low energy intensity and emission [3]. By applying this technique, work by Martinez has been able to reduce the weight of connecting rods to 33% [6] and Sulamet-Ariobimo to 27% [7]. Thin wall casting technology was applied to automotive components for the first time by Martinez [6] in hollow connecting rods and racing car front uprights. This technology was followed by Fraś et al. in wheel rims [8], cantilevers, rotor, and control arms [5]. Sulamet-Ariobimo applied this technique to produce a connecting rod for Vespa PX150 [7].

In thin wall casting technology, to reduce the weight, the thickness of the original component is reduced in whole or several parts of the area [5,6]. This process could disturb the mechanical properties. Whereas the substitute components should fulfill the requirements of the design.

This paper discusses the effects of reducing the I-beam surface from 4 mm to 3 mm and 2 mm on the mechanical characterization requested by Vespa PX150; since this work is part of serial works to develop a lighter connecting rod to substitute the original connecting rod of Vespa PX150 so that it would reduce the weight.

Reducing the weight of connecting rod was first done by Martinez et al. [6]. They reduced the weight of the connecting rod from 600 g to 400 g. The weight reduction is done by hollowing the I-beam which made the wall thickness in the I-beam reduced from 4 mm to 3 mm. This reduction results in a component weight loss of 33%. Following the work of Martinez et al. [6], Sulamet-Ariobimo et al. is developing a simpler casting design that can produce thin wall connecting rods [7]. In their design, Sulamet-Ariobimo et al. are avoiding the use of a hollowing mechanism to prevent the use of core during manufacturing. Furthermore, the design developed by Sulamet-Ariobimo et al. produces more than 1 connecting rod from 1 casting mold.

As mentioned previously, reducing the thickness of components should not disturb the mechanical properties. Mechanical properties could be disturbed by the changing in mechanical properties at the finding Colin-García et al. [9]. They found that nickel addition of 0,88 wt% will suppress the cementite formation and improve nodule count and nodularity while Omran et al. [10] found that if the carbon equivalent (CE) value increased then the hardness, UTS, and yield strength will be increased but the elongation will be decreased. As for the same percentage of CE values, the increase in casting thickness will decrease the hardness, UTS, and yield strength but increase the elongation. Elbana et al. [11] found in 2020 that nodule count, pearlite content, and interaction between both have a significant effect on tensile strength. When the pearlite content and nodule count decrease the UTS and yield strength will also decrease. Elongation and impact values will increase as UTS and yield strength decrease. Jhaveri et al. [12] stated that thin wall ductile cast iron can provide weight reduction comparable to

aluminum while having better mechanical properties. Using three light weighting cases: a different casing an engine block, and a replacement of cast iron parts. Jordan [13] redesigned the prototype of valve components from ductile iron (DI) casting in green sand to thin wall ductile iron (TWDI) in lost foam in 2020.

The focus of this work is on analyzing the effects of 3 mm and 2 mm I-beam thickness on the microstructures and compression load. This work also examines the repeatability of the casting design built to produce the connecting rods.

2. Materials and methods

This work is a part of a continuous research series, as presented in Fig. 1, which started with the making of TWDI plates to determine the casting pattern and characterization. Then the casting design is applied to produce TWDI automotive components. All the research is industrial based. The casting design developed by Sulamet-Ariobimo [7] is presented in Fig. 2. This design is the development from TWDI plates casting design IDP000039503 [14], IDP00040306 [15], and P00201600907 [16]. It is a vertical casting resulting in 4 connecting rods for each mold.

The dimension of the connecting rod is presented in Fig. 3. During the process at PT. Geteka Founindo, 2 types of the connecting rod were made. The difference between the two types of connecting rods lies in the thickness of the I-beam, which is 3 mm and 2 mm. The number of total samples is sixteen pieces.

Commercial liquid metals of FCD450 were used to produce all the connecting rods and came from 3 different pouring batches. This condition was planned to test the repeatability of the casting design. The first batch, known as P1, produced connecting rods with the thickness of the I-beam of 3 mm. The number of connecting rods produced was 8 pieces. The second batch, known as P2 produced I-beam thicknesses of 2 mm and 1 mm. The numbers of connecting rods produced were 4 for 2 mm and 4 for 1 mm. The third batch (P3) also has the same parameters as the second batch. The total samples were 8 for connecting rods with 2 mm I-beam thickness as well as 1 mm I-beam thickness.

The tapping temperature was around 1500 °C to 1400 °C for liquid treatment in the ladle. The liquid treatment was conducted in a 15 kg ladle using the sandwich method. Inoculant and nodulariser were placed together at the bottom of the ladle and covered up with steel scrap. The pouring temperature was around 1366 °C to 1395 °C with a pouring time of 4–5 s for every mold. The tapping and pouring temperatures used in this research were based on the requirement of the commercial products. The casting was discharged after 3–4 h and cleaned using a sandblasting process. The cleaning process is then followed by the machining process to separate the products with the gating system and risers. In this research, the liquid metal was produced using a 1200 kg induction furnace. The charging material is home scrap, steel scrap, ferrosilicon as carburize, FeMn, and FeSi. The pouring temperatures were 1404 °C, 1395 °C, and 1388 °C. There are differences in pouring

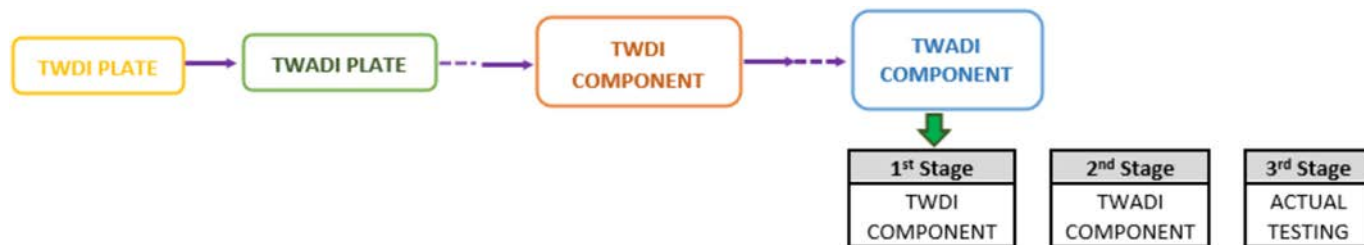


Fig. 1. Roadmap research.

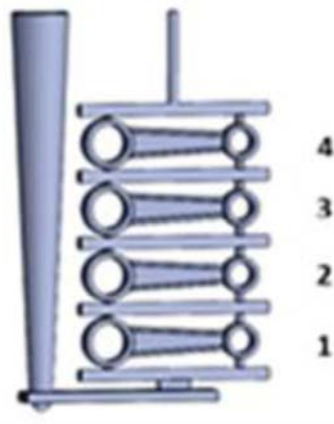


Fig. 2. Casting design.

temperature but all the pouring temperatures are still beyond the foundry standard. Information and coding for each connecting rod can be found in Table 1. The chemical composition of each pouring can be seen in Table 2.

The chemical composition of the liquid metal was analyzed with spectrometry. While all the connecting rods were subjected to a compression test using Geotech AI – 7000 LA10 Servo Control Computer System Universal Tensile Machine with a maximum load capacity of 10,000 kg. The test was run directly on the rod using a special holder as presented in Fig. 4. The compression test was run following the tensile testing method with reversed load direction. The compression rate was 20 mm/min. Compression load and deflection were recorded as the data. After the compression test, the cross-section of each I-beam was subjected to metallographic examination. The metallographic samples were taken from the I-beam and the end rod area as presented in Fig. 5. After the cutting

and mounting processes, the surface of every sample was analyzed using a magnifying tool that enlarged the surface six times.

3. Results and discussion

As presented in Fig. 6, casting defects are not formed in connecting rods produced in P1. However, the same result does not occur in P2 and P3, as can be seen in Figs. 7 and 8. Shrinkage appeared in all I-beams with a thickness of 1 mm but not in the I-beams with a thickness of 2 mm. An investigation was conducted, and the result showed that during the pouring process, the flow of molten metal that entered the mold had stopped for a few seconds due to changes in the movement of the foundryman in charge. This lack of heat which was brought by the molten metal made the ingate freeze and the risers fail to perform their function. This finding confirms that solidification will not begin if there is still molten metal flow in the gating system. Due to this finding, the pouring process must continue until the mold is filled. The slightest disturbance to the filling process will cause premature solidification which will damage the casting product.

Table 2 presents the chemical composition of each pouring batch. When these results are compared to the foundry standard, it is seen that all the testing results fulfill the requirement except for sulfur, copper, and molybdenum contents. Sulfur in P1 and P2 is 33% higher than that of the foundry standard. The content of copper in all pouring exceeds the foundry standard for 53%, 80%, and 27% for P1, P2, and P3, respectively. As for molybdenum, the foundry standard does not mention its limitation. Molybdenum is a ferrite stabilizer with a strong affinity to carbon [17]. Avila et al. [18] mentioned that molybdenum will affect the iron if the content reaches 0.5%. While Chen et al. [19] mentioned that graphite shape and amount will be disturbed if the molybdenum content is minimally 0.5%. Molybdenum content in P2 is 0.002%. So, the Molybdenum will not disturb the iron.

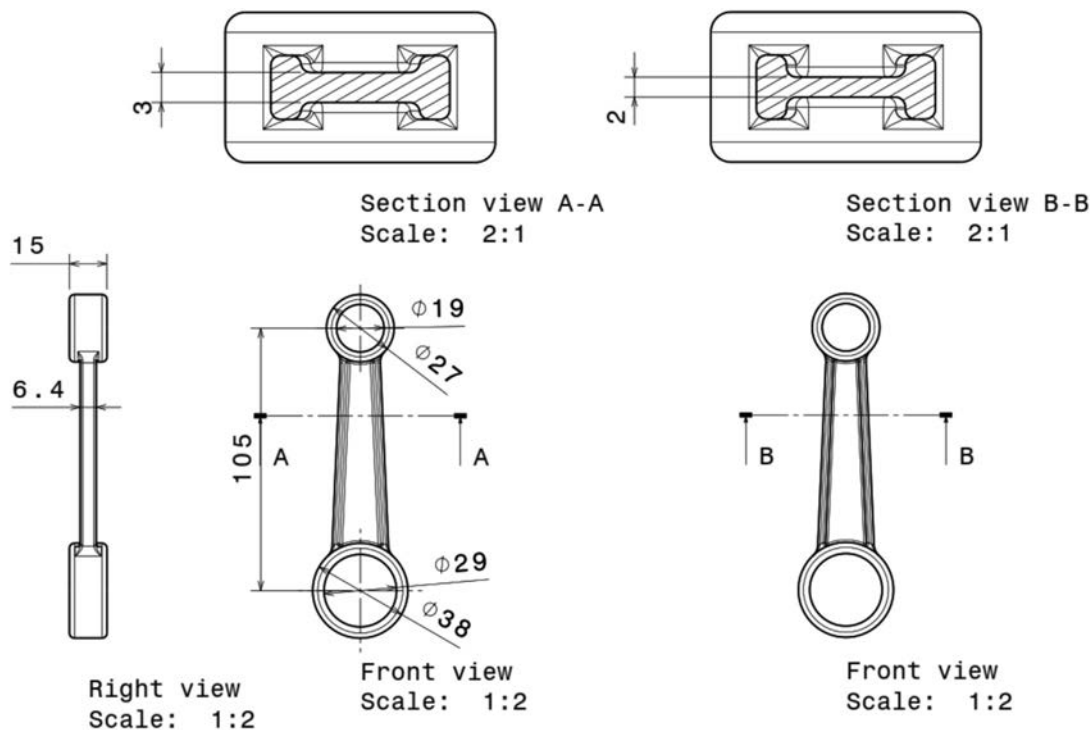


Fig. 3. Design of connecting rod.

Table 1
Information and coding of connecting rod.

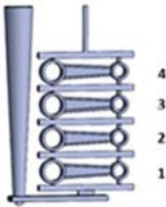
Pouring batch	Thickness (mm)	Sample code		Pouring batch	Thickness (mm)	Sample code	Position		
For P1	3	1		P2	2	A	1		
		2				B	2		
		3				C	3		
		4				G	4		
		5				P3	2	D	1
		6						E	2
		7						F	3
		8						H	4

Table 2
Chemical composition.

Element		Standard (wt%)		Testing result (wt%)		
		ASTM	Foundry	P1	P2	P3
Carbon	C	3.6–3.8	3.5–4.0	3.62	3.68	3.82
Silicon	Si	1.8–2.8	2.4–2.8	2.54	2.69	2.66
Manganese	Mn	0.15–1.00	0.3–0.5	0.42	0.45	0.40
Magnesium	Mg	0.03–0.06	min. 0.03	0.04	0.06	0.04
Phosphor	P	max. 0.30	max. 0.03	0.02	0.02	0.01
Sulfur	S	max. 0.02	max. 0.015	0.02	0.02	0.01
Copper	Cu	0.015–1.00	max. 0.15	0.23	0.27	0.19
Chromium	Cr	0.03–0.07	max. 0.15	0.09	0.04	0.06
Nickel	Ni	0.05–2.00	max. 0.02	0.007	0.01	0.002
Molybdenum	Mo	0.01–0.10	–	0.00	0.002	0.00
CE (%)				4.47	4.38	4.71
CE Calc – 1	%C + 0.31%Si			4.41	4.51	4.65
CE Calc – 2	%C + 0.31%Si + 0.55%P – 0.027%Mn + 0.4%S			4.42	4.52	4.64

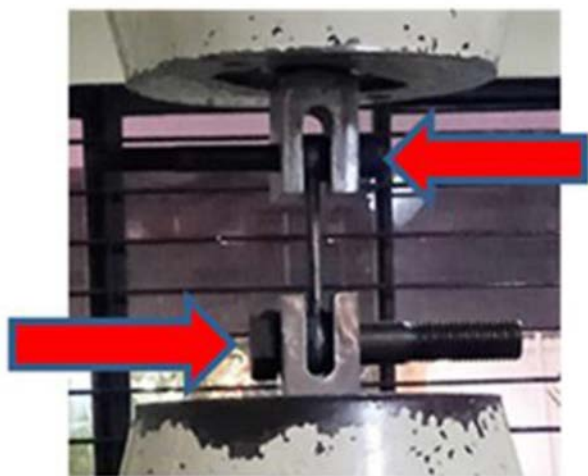


Fig. 4. Special holder for compression test.



Fig. 5. Position for metallography examination.

Different results were found when comparing the chemical composition with ASTM standards. Based on the ASTM standard, sulfur content reaches its maximum limit, copper content stays in the limits, and molybdenum content is below the minimum standard limit of 80%–100%. Except for molybdenum, special notice should also be given to carbon, chromium, and nickel. The carbon content in P3 is 0.5% higher than the maximum limit. Chromium content in P1 has exceeded the maximum limit of the ASTM standard by 29%, while the nickel content is 86%, 80%, and 96% below its minimal limit for P1, P2, and P3. These different considerations can be understood since ASTM provides a more general standard and most of the problems that occurred within the foundry standard

are covered by ASTM standard, and thus, further discussion will be carried out regarding the ASTM standard.

The analysis results based on ASTM standards for sulfur and copper are still in the limit, while molybdenum for all pouring is 80%–100% below the minimum limit, carbon in P3 is 0.5% higher than the maximum limit, chromium content in P1 is 29% higher than the maximum limit and nickel, in all pouring, is 80%–96% below the minimal limit. Based on these results, due to less nickel but high copper contents, the matrix formed within all casting would tend to have a pearlite composition. P3 would have the highest nodule count whereas carbide formation would be high in P1. Nickel and molybdenum are elements that will improve hardenability [17], however, in this work, since austempering is not performed in this part, the effect could not be seen.

When the chemical composition between the pouring is compared, P3 has the most unsatisfied requirements. It has the highest carbon content which means it will have the highest nodule formation compared to the other two batches. However, P3



Fig. 6. Products of P1.



(1) P2 – 2 mm



(2) P2 – 1 mm

Fig. 7. Products of P2.



(1) P3 – 2 mm



(2) P3 – 1 mm

Fig. 8. Products of P3.

has the lowest copper content, which is a graphite former. Thus, with this combination, the addition of nodule graphite will not be too significant. P2 has the highest silicon content but it also has the highest manganese content. Silicon and manganese have a reversal function, and hence, the combination in P2 could give the same result as the other batches. Since P2 has the highest magnesium content, it will have the highest nodularity.

The testing result of CE values shows that all values are above 4.3. This means that all are hyper-eutectic nodular cast irons. The differences in CE value between batches are 2%–7%. The highest CE value is found in P3 while the lowest is in P2. The CE value resulting from the calculation shows 3% higher than the result of spectrometry. Since the CE value is closely related to the presence of carbide and primary graphite, then the confirmation process will be

carried out by examining the microstructure results regarding the presence of carbide and primary graphite. As for the graphite floatation, the nodule graphite will not float due to the CE value [20].

CE can be used to determine the type of cast iron [16]. In addition, CE value also has an important role in carbide formation [21]. Martínez suggested having CE values of 4.4–4.6 to obtain free carbide nodular cast iron [6] and Stefanescu suggested above 4.3% [22]. Based on the work of Martínez, P1 and P3 will have carbide free [6], whereas based on the work of Stefanescu, all batches will have carbide free. Different considerations were found in the work of Soedarsono et al., who also found that CE is not the only factor to determine carbide-free condition since their work showed that carbide was still not formed in a CE value of 4.2 but found in a CE value of 4.6 effect [23].

Fig. 9 presented the metallographic specimens before they were prepared for metallographic examination. The analysis of each surface indicates that every surface has its own color pattern such as in Figs. 9–4 and 9–H. Fig. 9 also reveals the difference in color patterns between the I-beam and the end rod. This indicates that the matrix of the microstructures is not uniform in every sample and connecting rod. Bright or white color represents the presence of carbide while the dull or grey color represents the presence of pearlite or pearlite-ferrite matrix. This could happen due to cooling rate differences caused by the thickness and casting design. The cooling rate of carbide is higher than that of pearlite or pearlite-ferrite matrix. Fig. 9 also shows the presence of defects in C, D

and F. Based on the shape of the defects, there are some assumptions regarding what may cause the defects, which are impurities carried away by the liquid metal during pouring, liquid metal erosion, or the mold condition. Further analysis showed that the defects were caused by impurities carried in the molten metal.

A schematic illustration of the solidification process performed in Fig. 10(a) [24] shows that during the solidification process, heat represented by a red arrow will leave the molten metal through all its sites. Solidification rates are determined by the surface area and condition of each site. If the area and condition of all the sites are the same, then the solidification rate will also be the same. Fig. 10(b) gives a schematic illustration of the heat leaving direction for the casting design. This schematic illustration shows that the heat leaving directions collides with each other except for the right side. This condition disturbs the solidification rate.

Fig. 10(c) [25] presents a simulation of the solidification process for 3 mm, 2 mm, and 1 mm thicknesses. The simulation shows different solidification patterns for each thickness, but all solidification started at the center of the I-beam and proceeded to the end rod. This shows similarity with the schematic illustration given in Fig. 10(a), especially Fig. 10(b).

The result of metallographic examinations is shown in Fig. 11. In general, the un-etched microstructures reveal that the nodule graphite was distributed evenly for both I-beam and end rod areas for all CE conditions. The nodule count in I-beam seems to be higher than that of the end rod. The nodule size also looks finer in I-beam compared to that of the end rod. Several defects were found in both

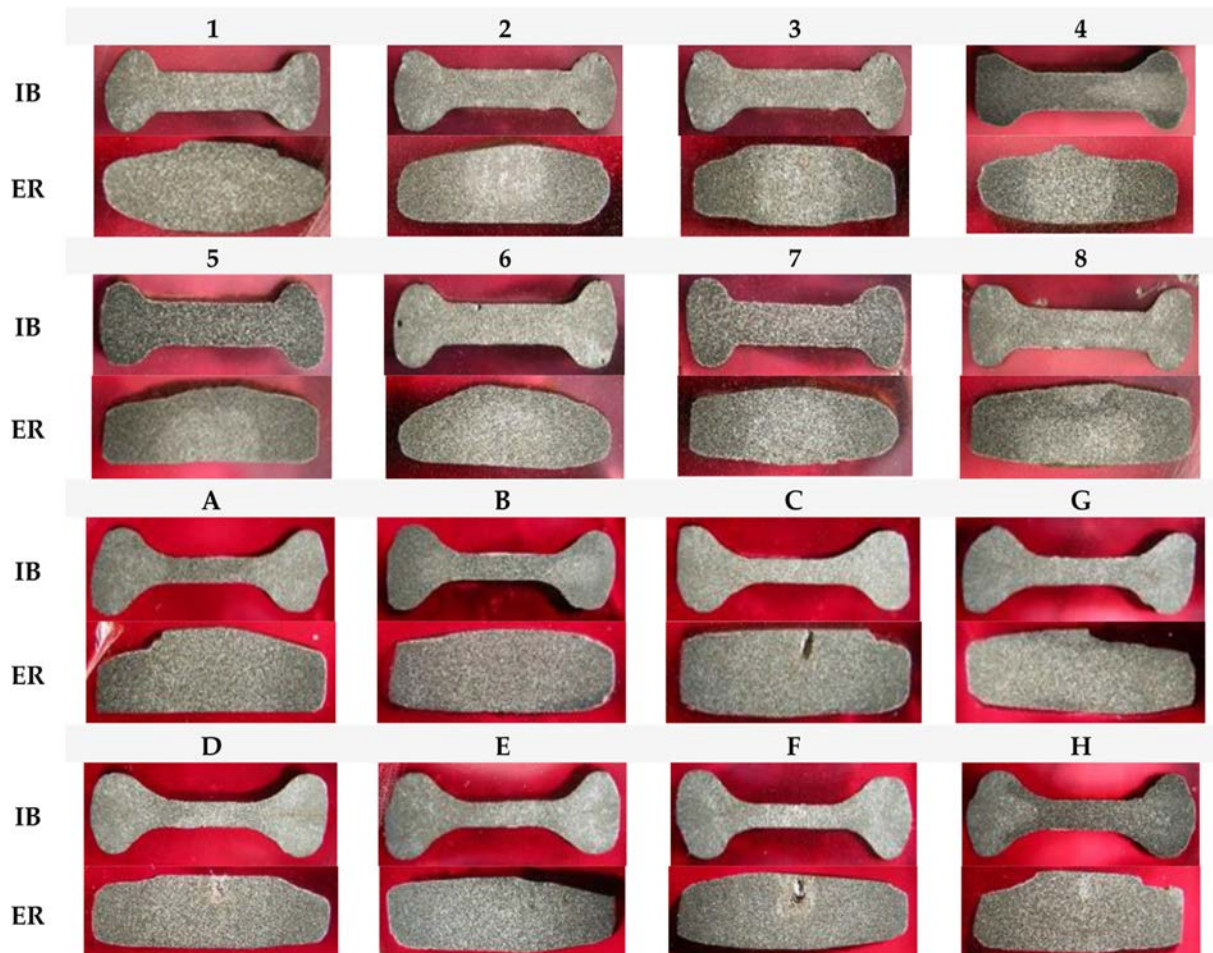
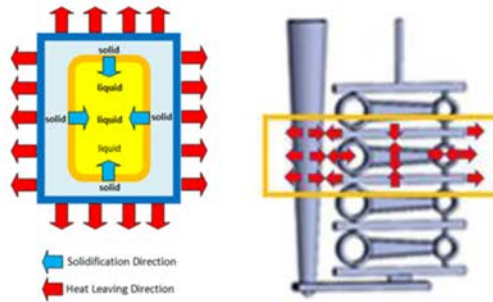
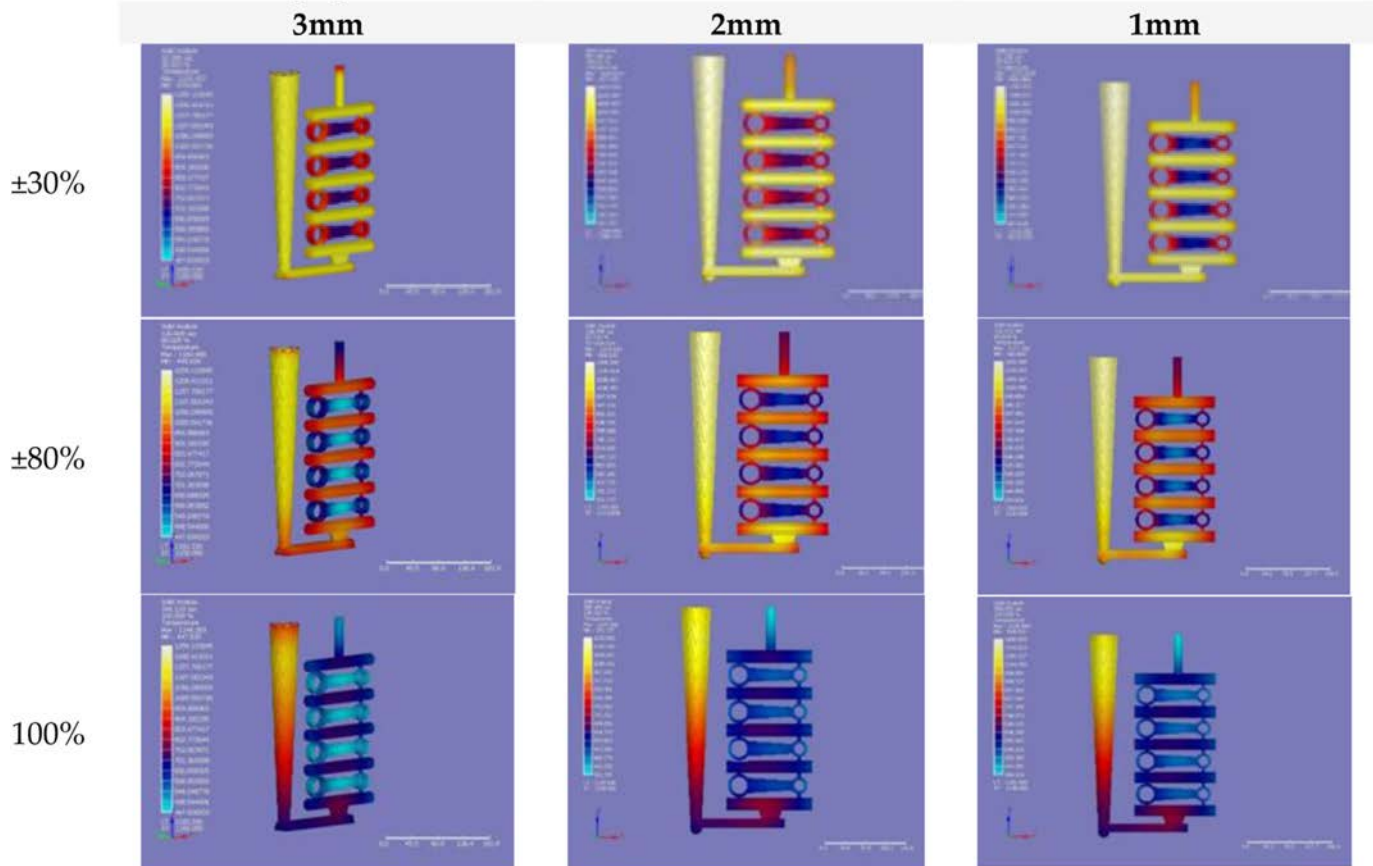


Fig. 9. Macro examination of connecting rod (M-6x). IB = I-beam and ER = end rod.



(a) Schematic Illustration of Solidification Process [24]. (b) Schematic Illustration of Heat Leaving Direction



(c) Simulation Comparison of Solidification Process [25]

Fig. 10. Effect of casting design on cooling rate.

I-beam and end rod. The defects in I-beam are not casting defects, they are formed during the compression test as can be seen in Fig. 12. On the contrary, the defects in the end rod are casting defects that will be revealed in the surface examination.

Un-etched microstructures of the connecting rod with an I-beam thickness of 2 mm do not exhibit any irregularity, only the presence of primary graphite in the end rod of sample H, as presented in Fig. 13. It is normal since the CE value for this sample is 4.71. The connecting rod with an I-beam thickness of 3 mm must be considered due to the finding of similarity of the nodule size between the I-beam and the end rod area for samples 4, 5, and 7. This will be confirmed in the quantitative analysis. The etched microstructures reveal that there is a difference in the matrix formed on the I-beam with the end rod and there is a mixed matrix found in

both the I-beam and the end rod. This finding supported the result of the macro examination of the color pattern in each sample of the I-beam and the end rod surfaces. The etched microstructure also supported that bright or white color in the macro examination is carbide and dull or grey color is pearlite or ferrite-pearlite matrix. Apart from nodule graphite, etched microstructures reveal the presence of carbide, pearlite, and ferrite-pearlite.

In the connecting rod with the I-beams thickness of 2 mm, the microstructure of the I-beam is different from the one in the end rod. The microstructure in the I-beam is a mixture of nodule graphite and carbide in a pearlite matrix, while in the end rod is nodule graphite in a ferrite-pearlite matrix. Specialties are found in samples G and H. As presented in Fig. 14, the microstructure in the I-beam is like the one in the end rod. In sample G, the microstructure is nodule graphite

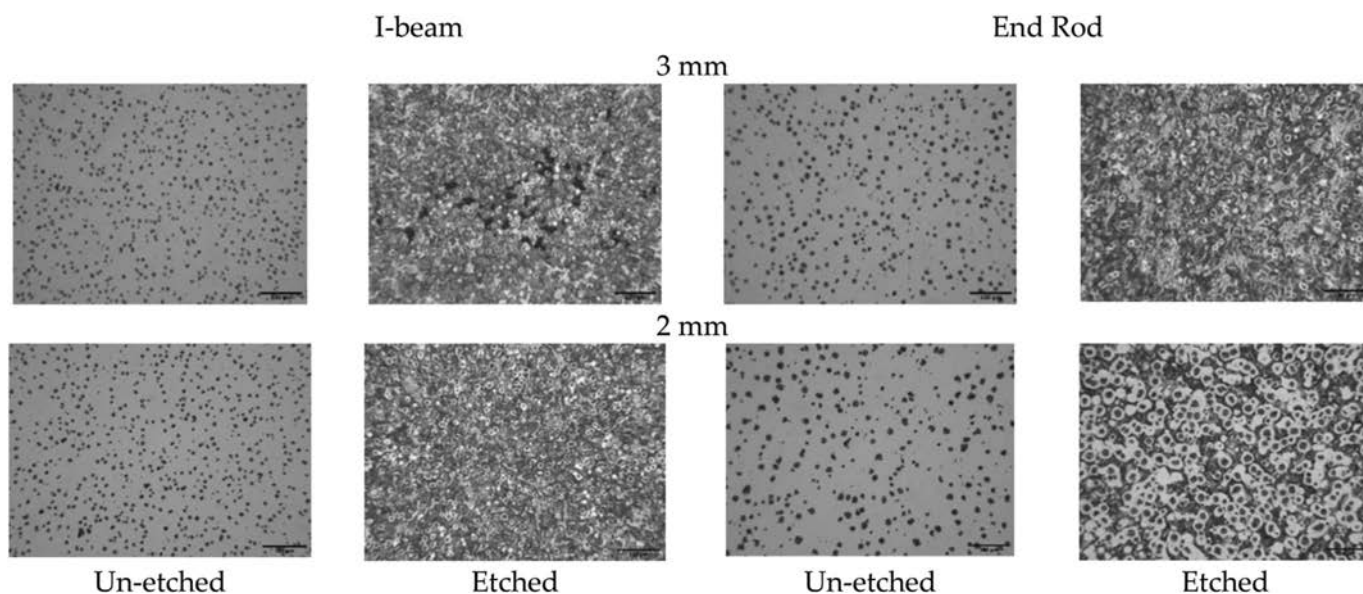


Fig. 11. Microstructures.

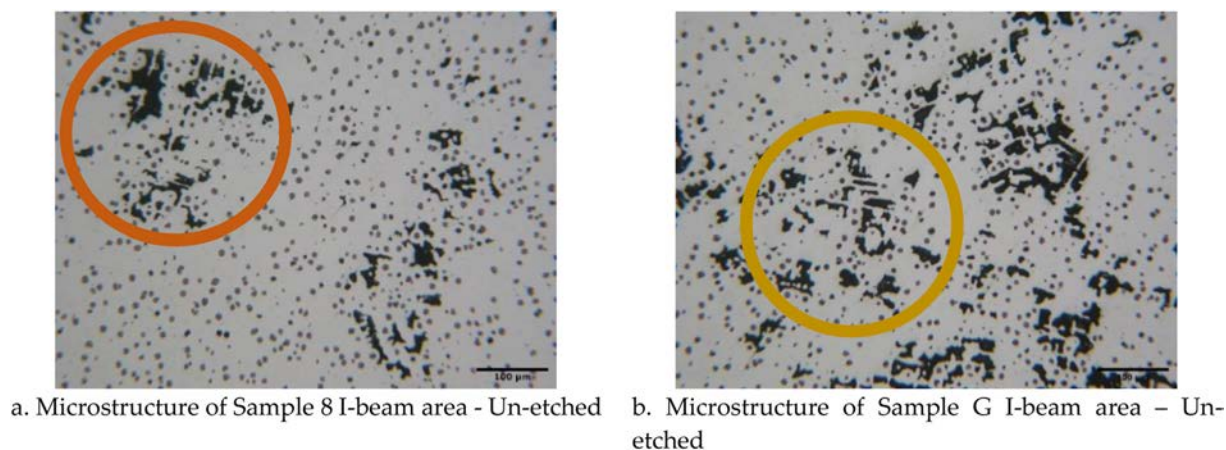


Fig. 12. Deformation trace after the compression test.

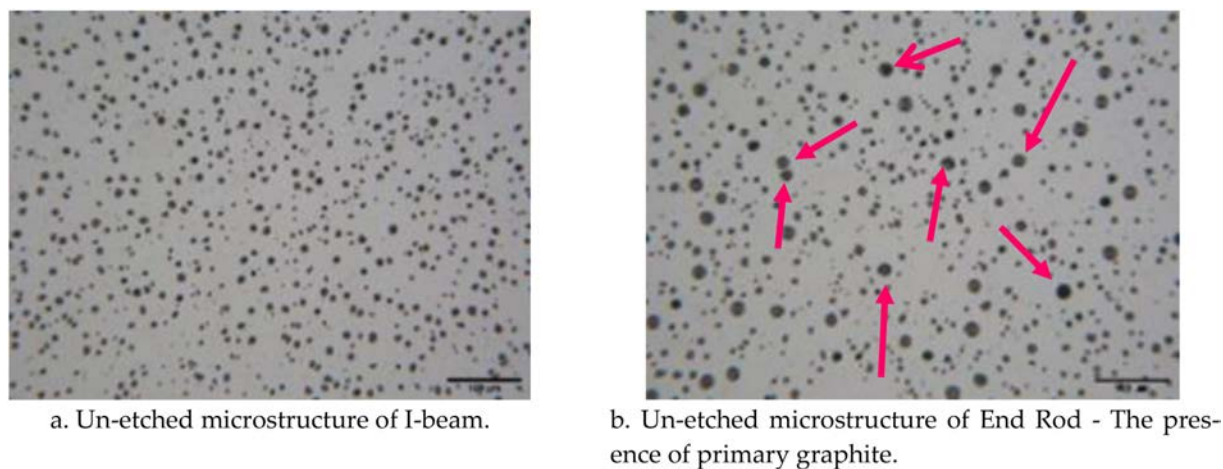


Fig. 13. Un-etched microstructures of sample H— 2 mm I-beam thickness.

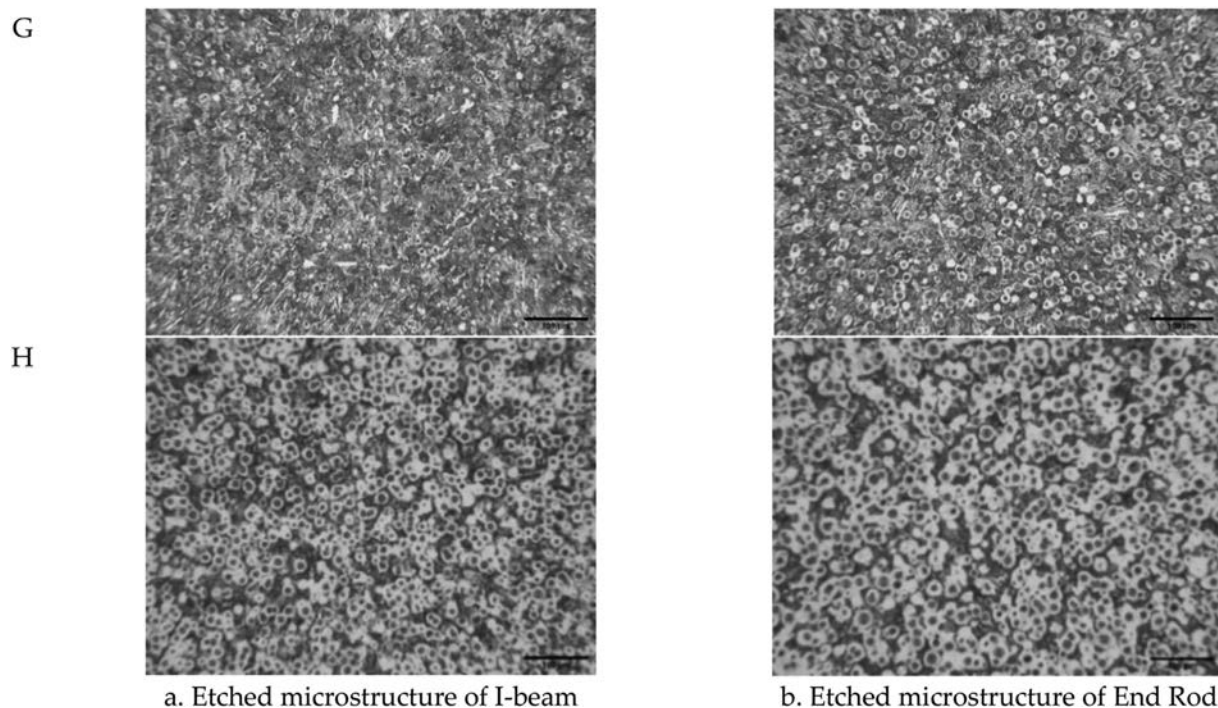


Fig. 14. Etched microstructures of sample H—2 mm I-beam thickness.

with carbide in a pearlite matrix, meanwhile, in sample H, the microstructure is nodule graphite in the ferrite-pearlite matrix. This is expected to be due to the CE value.

As for the 3 mm I-beam, differences between the I-beam and the end rod are also observed. The microstructure of the I-beam in Sample 1 is like its end rod, which is nodule graphite with carbide in a pearlite matrix. Similar conditions are also found in Samples 3 and 4 but with different microstructures. There are 2 types of microstructures in both I-beam and end rod as presented in Fig. 15. The microstructures are nodule graphite with carbide in a pearlite matrix and nodule graphite in a ferrite-pearlite matrix.

As for the rest, the microstructure in the I-beam is different from the one in the end rods. Nodule graphite with carbide in a pearlite matrix is obtained in the end rod for samples 2, 6, and 8, while the I-beam microstructure consists of nodule graphite in a ferrite-pearlite matrix and nodule graphite with carbide in a pearlite matrix. For sample 5 and 7, the I-beam microstructure is nodule graphite in a ferrite-pearlite with ferrite dominant, while the end rod microstructures consist of nodule graphite with carbide in a pearlite matrix as shown in Fig. 16. This finding confirms the surface examination. Further, the presence of carbide in every microstructure confirms the finding of Soedarsono et al. [23], while the formation of pearlite and ferrite-pearlite matrix confirm the assumption regarding the lack of nickel and the excess of copper content mentioned previously.

Fig. 17 presents the nodule count. As assumed previously, the nodule count in the I-beam would be higher than that of the end rod except for sample 7. This is expected due to the thickness differences of the I-beam. To reduce the weight of the connecting rod, the I-beam thickness was reduced while the end rod thickness was constant. As for sample 7, the un-etched microstructure has a similar size of nodule graphite in the I-beam and the end rod, which is unusual. A similar nodule graphite size also occurs in sample 5. Further investigation is yet to be carried out to reveal the cause of this anomaly.

Based on the thickness, the number of nodules counted in the 2 mm thickness I-beam should exceed the one in the 3 mm thickness I-beam. However, the quantitative result revealed a different result. The explanation for this discrepancy could be due to an imprecise measure of the cooling rate.

Fig. 18 shows the compression test results of the connecting rods for 3 mm and 2 mm I-beam thickness. They consist of compression load on the y -axis and deflection on the x -axis. Both diagrams are divided into 2 areas, which are elastic and plastic areas. The load–deflection diagrams were not converted to stress–strain diagrams because the cross sections of the specimens are not constant along the length and the surface area for both specimens is different. Although the values for both compression load and deflection for 2 mm and 3 mm thickness differ, no substantial difference was observed. For both diagrams, the elastic deformation area shows a linear line until plastic deformation commences and progresses nonlinearly. No clear distinction can be made between elastic and plastic deformation areas. The plastic deformation progresses through the curve peak until rupture. At the curve peak which is corresponding to the maximum load, crack initiation may be occurred and propagated with decreasing load until rupture.

The diagrams show that the maximum load for 3 mm is 4906 kg with 2.67 mm of deflection. While for the 2 mm I-beam thickness, the maximum compression load is 3818 kg with a deflection of 3.36 mm. Maximum compression load for the 3 mm I-beam thickness is 29% higher than 2 mm with a deflection of 21% shorter. As for rupture load for 3 mm is 4650 kg with 2.91 mm deflection. Whereas the rupture load for I-beam with 2 mm thickness is 3280 kg with 3.84 mm deflection. The rupture load of 3 mm thickness is 42% higher than 2 mm with a 24% deflection shorter. The diagrams also reveal the approximately highest load limit of elasticity is 1100 kg with 1.24 mm deflection for an I-beam thickness of 3 mm and 1520 kg with 2.24 mm deflection for a 2 mm I-beam thickness. These findings show that the I-beam with a 2 mm thickness is more ductile than the 3 mm thickness. The I-beam with

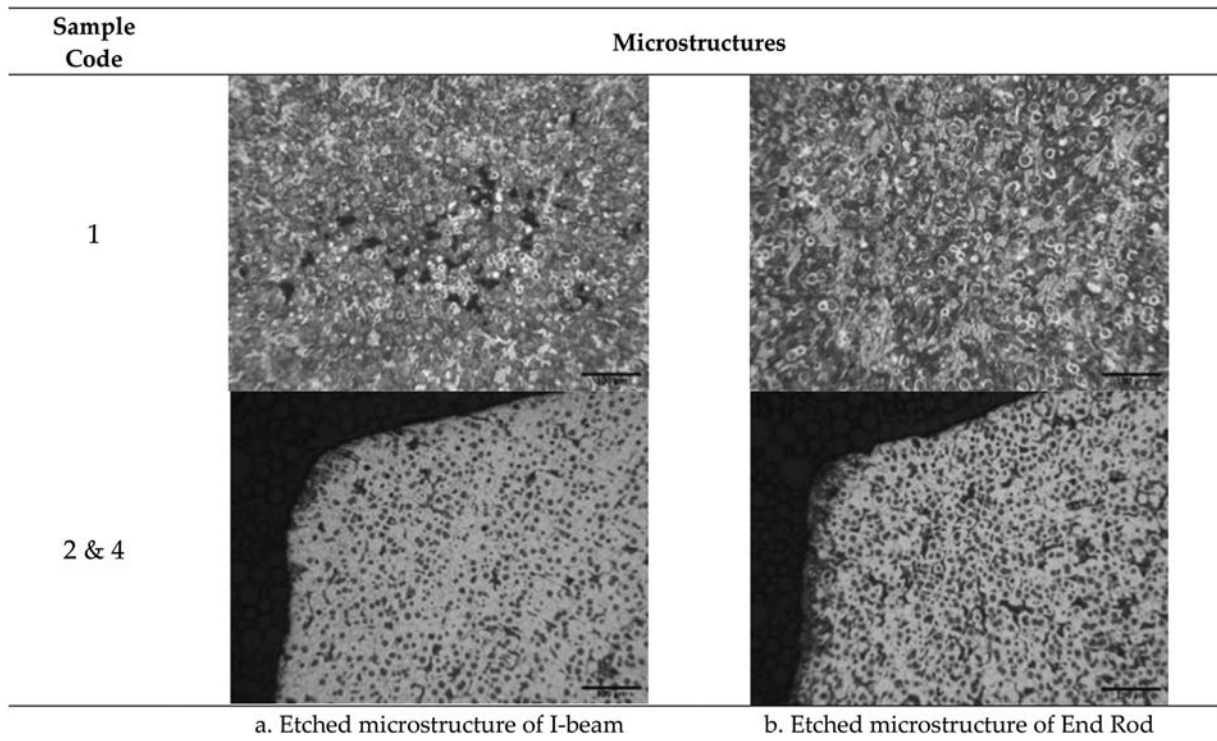


Fig. 15. Etched microstructures of connecting rod with 3 mm I-Beam thickness sample 1 (nodule graphite with carbide in perlite matrix), and sample 3 and 4 (nodule graphite in a ferrite-pearlite matrix).

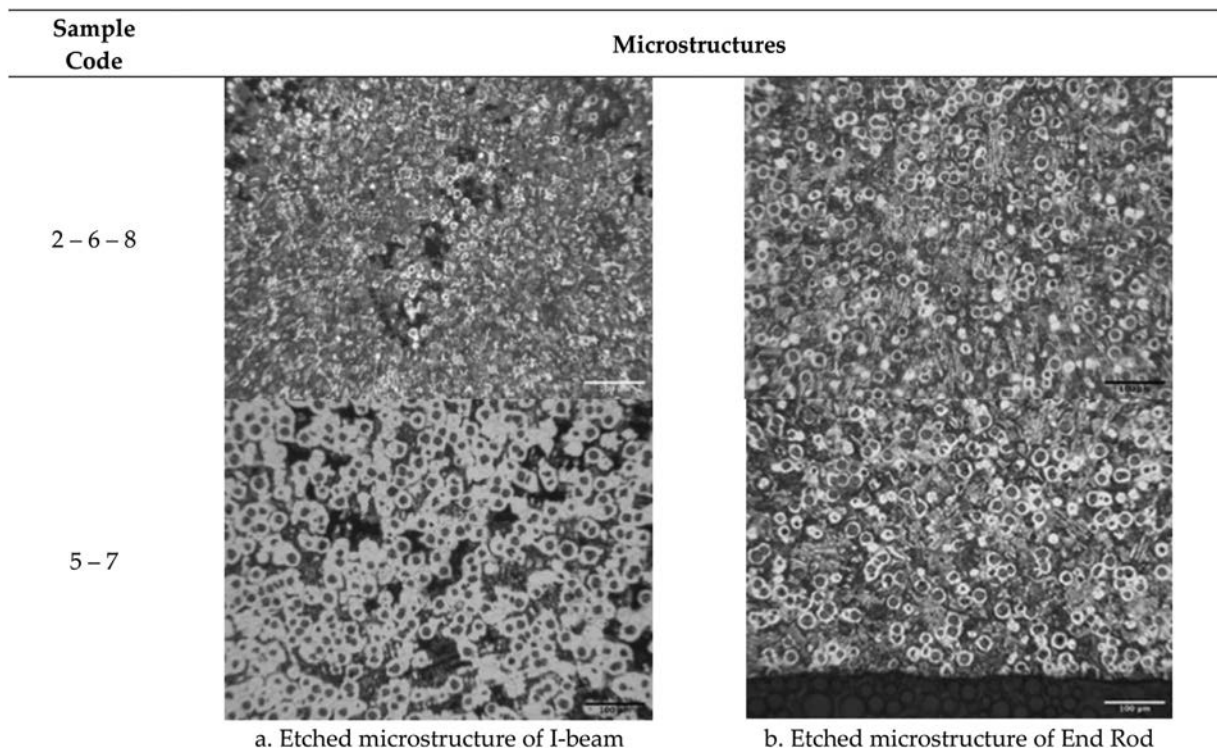


Fig. 16. Etched microstructures of connecting rod with 3 mm I-beam thickness sample 2,6, and 8 and sample 5 and 7.

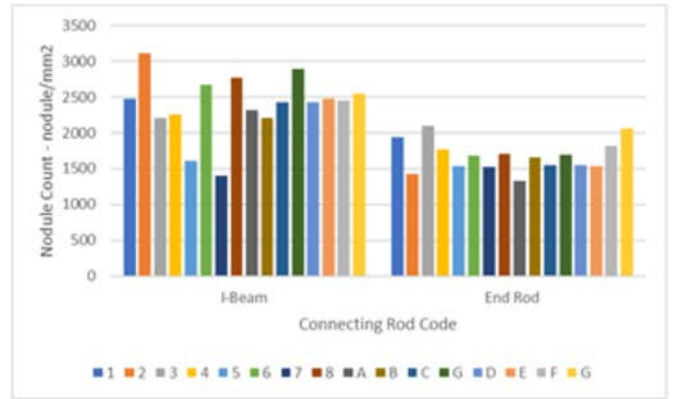
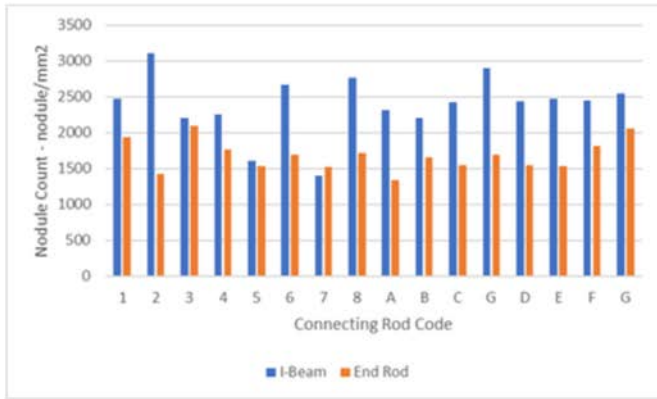
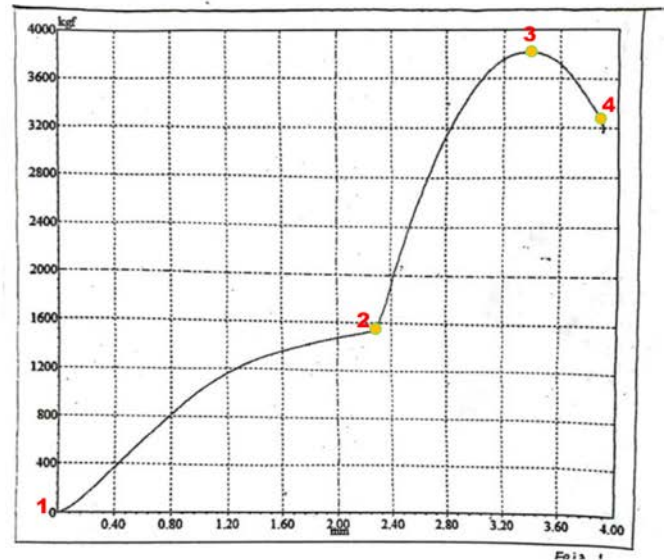
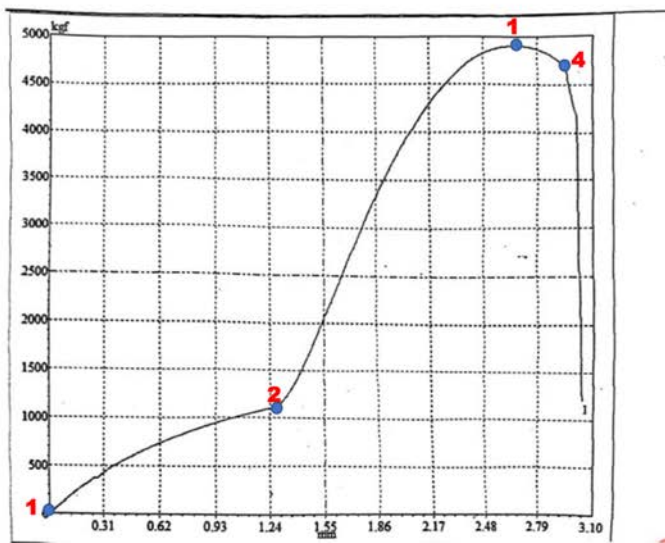


Fig. 17. Nodule count.



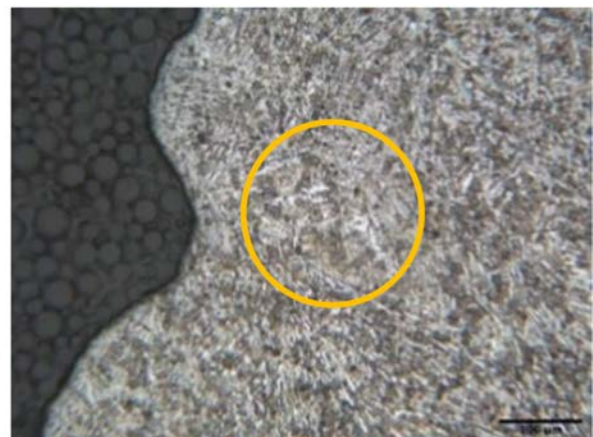
a. Result of Compression Test for 3 mm I-beam Thickness

b. Result of Compression Test for 2 mm I-beam Thickness

Fig. 18. Load–deflection diagram of I-beam compression test. 1 to 2 = elastic area, 2 to 4 = plastic area, 3 = maximum load, 4 = rupture.



Sample 1 - Etched



Sample 2 - Etched

Fig. 19. Microstructures of broken sample 1 and 2.

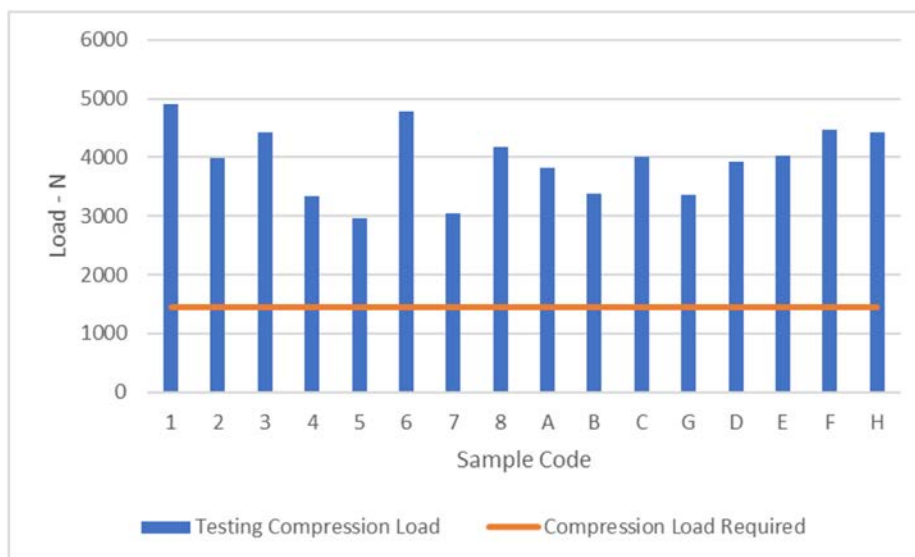


Fig. 20. The result of compression test.

a 2 mm thickness has a higher yield point but the 3 mm thickness has a higher ultimate compression load.

Of all the connecting rods, only sample numbers 1 and 2 were broken. This is expected due to the presence of carbide as can be seen in the etched microstructure of Fig. 19. Carbide makes the connecting rod brittle and breaks during the compression test. The rest of the samples just bend.

The compression loads for all the connecting rods are given in Fig. 20. All the compression loads are above the requirement, which is 1455 N. The average compression load from the connecting rod with 3 mm I-beam thickness is 3955 N and the average from 2 mm I-beam thickness is 3927 N. The difference in the average compression load is 0.7%, which is not significant. Thus, the compression load can be the same. This result is in line with the finding obtained in our previous research [26], which was 3525 N.

4. Conclusions

The repeatability of casting design established to produce connecting rod with 3 mm I-beam thickness has been proven. The 3 mm I-beam connecting rod has been reproduced 7 times with this work and still gives constant result in microstructure and compression load. As for the design of connecting rod with 2 mm I-beam thickness has been reproduced once and for two times production, the results are also stable. Lack of nickel combined with exceeded copper will result in pearlite or ferrite-pearlite dominant pearlite matrix. These conditions have been confirmed by the etched microstructure which is dominated by the presence of pearlite matrix. This work also found inhomogeneous microstructure in I-beam and end rod. It is also found that most of the connecting rods have different microstructure condition between I-beam and end rod. This problem can be solved by austempering process.

The results of compression load for both 2 mm and 3 mm I-beam thickness show that both connecting rods have similar compression load and above the requirement need by the original connecting rod.

Conflict of interest

The authors whose names are listed immediately below certify that they have NO affiliations with or involvement in any

organization or entity with any financial interest (such as honoraria; educational grants; participation in speakers' bureaus; membership, employment, consultancies, stock ownership, or other equity interest; and expert testimony or patent-licensing arrangements), or non-financial interest (such as personal or professional relationships, affiliations, knowledge or beliefs) in the subject matter or materials discussed in this manuscript.

Acknowledgment

The authors wish to show their gratitude to Universitas Trisakti for the research grant, PT. Geteka Founindo, CFMA-FTUI and to all parties who have supported this research.

References

- [1] P. Davis, M. Robinson, B. Jackson, J. Wicker, Gov 2 | Vehicle Technologies Program, 2015 [Online]. Available: www.eia.gov.
- [2] Julian M. Allwood, Jonathan M. Cullen. Sustainable materials: With both eyes open, UIT Cambridge, 2011.
- [3] M. Jolly, K. Salonitis, Primary manufacturing, engine production and on-the-road CO₂: how can the automotive industry best contribute to environmental sustainability?, 38th International Vienna Motor Symposium, April 2017, pp. 27–28 (Vienna, Austria).
- [4] F. Czerwinski, Current trends in automotive lightweighting strategies and materials, Materials 14 (21) (2021), <https://doi.org/10.3390/ma14216631>. Nov.
- [5] E. Fraś, M. Górny, H. Lopez, Thin wall ductile iron castings as substitutes for aluminium alloy castings, Arch. Metall. Mater. 59 (2) (2014) 459–465, <https://doi.org/10.2478/amm-2014-0076>.
- [6] R. Martínez, R.A. Martínez, R.E. Boeri, J.A. Sikora, Experimental y modelado computacional multi-escala View Project Applications of ADI in High Strength Thin Wall Automotive Parts, 2002. Accessed: Nov. 17, 2022. [Online]. Available: <https://www.researchgate.net/publication/266186440>.
- [7] R. Sulamet-Ariobimo, G. Yudha, T. Sukarnoto, Y. Mujalis, Y. Oktaviano, Thin Wall Austempered Ductile Iron Connecting Rod for Lighter Automotive Component-Production of Thin Wall Ductile Iron Connecting Rod, SAE, 2017. Technical Paper.
- [8] E. Fraś, M. Górny, W. Kapturkiewicz, Thin wall ductile iron castings: technological aspects, Arch. Foundry Eng. 13 (1) (2013) 23–28, <https://doi.org/10.2478/afe-2013-0005>.
- [9] E. Colín-García, A. Cruz-Ramírez, G. Reyes-Castellanos, J.A. Romero-Serrano, R.G. Sánchez-Alvarado, M. Hernández-Chávez, Influence of nickel addition and casting modulus on the properties of hypo-eutectic ductile cast iron, J. Min. Metall. B Metall. 55 (2) (2019) 283–293, <https://doi.org/10.2298/JMMB181012023C>.
- [10] A.-N. Omran, G.T. Abdel-Jaber, A.-K. Abuel-Kareem, Mechanical properties of ductile cast iron at different carbon equivalent and cast thickness, IJRDO-Journal of Applied Science 5 (7) (2019) 24–34, <https://doi.org/10.53555/as.v5i7.3057>. Jul.

- [11] N. Elbanna, A. Nofal, A. Hussein, M. Tash, Mechanical properties of thin wall ductile iron: experimental correlation using ANOVA and DOE, in: *Key Eng. Mater.* vol. 835, KEM, 2020, pp. 171–177, <https://doi.org/10.4028/www.scientific.net/KEM.835.171>.
- [12] K. Jhaveri, G.M. Lewis, J.L. Sullivan, G.A. Keoleian, Life cycle assessment of thin-wall ductile cast iron for automotive lightweighting applications, *Sustainable Materials and Technologies* 15 (2018) 1–8, <https://doi.org/10.1016/j.susmat.2018.01.002>. Apr.
- [13] S. Jordan, M. DeBruin, Reducing the weight of vehicle components via lost foam casting of ductile and austempered ductile iron, 2020.
- [14] B. Suharno, J. Wahyuadi, T. Soemardi, R. Sulamet-Ariobimo, The effects of plates position in vertical casting producing thin wall ductile iron, *Adv. Mater. Res.* 277 (Nov. 2011) 66–75, <https://doi.org/10.4028/www.scientific.net/AMR.277.66>.
- [15] R. Sulamet-Ariobimo, J. Wahyuadi, Effect of plate thickness and casting position on skin effect formation in thin wall ductile iron plate, *International Journal of Technology* 7 (2016) 374, <https://doi.org/10.14716/ijtech.v7i3.2844>. Nov.
- [16] R. Sulamet-Ariobimo, Y. Gemilang, D. Dhaneswara, J. Wahyuadi, B. Suharno, Casting design modification to improve casting yield in producing thin wall ductile iron plate, *Mater. Sci. Forum* 929 (2018) 10–17, <https://doi.org/10.4028/www.scientific.net/MSF.929.10>. Nov.
- [17] E. Konca, K. Tur, E. Koç, Effects of alloying elements (Mo, Ni, and Cu) on the austemperability of GGG-60 ductile cast iron, *Metals* 7 (2017) 320, <https://doi.org/10.3390/met7080320>. Nov.
- [18] J. Hernandez-Avila, E. Salinas-Rodriguez, E. Cerecedo-Saenz, et al., The effect of molybdenum on the microstructure of nodular iron, *Eur. Sci. J.* 11 (36) (2015) 377–388.
- [19] X. Chen, Q.-J. Zhai, H. Dong, B.-H. Dai, H. Mohrbacher, Molybdenum alloying in cast iron and steel, *Adv. Manuf.* 8 (2019), <https://doi.org/10.1007/s40436-019-00282-1>. Nov.
- [20] D. White, Avoiding shrinkage defects and maximizing yield in ductile iron, *120* (2012) 389–398.
- [21] Casting, vol. 15, ASM International, 2008, <https://doi.org/10.31399/asm.hb.v15.9781627081870>.
- [22] D. Stefanescu, L.P. Dix, R. Ruxanda, C. Corbitt-Coburn, T.S. Piwonka, Tensile properties of thin wall ductile iron, *Trans. Am. Fish. Soc.* 110 (2002).
- [23] J.W. Soedarsono, T.P. Soemardi, B. Suharno, R.D. Sulamet-Ariobimo, Effects of carbon equivalent on the microstructures of thin wall ductile iron, *J. Mater. Sci. Eng.* 5 (2011) 266–270.
- [24] R. Sulamet-Ariobimo, J. Wahyuadi, B. Suharno, Cooling rate analysis of thin wall ductile iron using microstructure examination and computer simulation, *Appl. Mech. Mater.* 752 (753) (Dec. 2015) 845–850, <https://doi.org/10.4028/www.scientific.net/AMM.752-753.845>.
- [25] R. Sulamet-Ariobimo, S. Aziza, M. Fadhlán, Y. Oktaviano, Y. Mujalis, The application of thin wall ductile iron process in connecting rod, in: *International Conference on Mechanical Engineering for Emerging Technologies (In Progress)*, Nov 2021.
- [26] R. Sulamet-Ariobimo, M. Fadhlán, S. Kamili, T. Sukarnoto, Y. Mujalis, Y. Oktaviano, Effects of austempering process to mechanical properties of thin wall ductile iron connecting rod, in: *IOP Conf. Ser. Mater. Sci. Eng.* vol. 547, Dec 2019, p. 12051, <https://doi.org/10.1088/1757-899X/547/1/012051>.